p-FEM for finite deformation powder compaction

Ulrich Heisserer [a], Stefan Hartmann [b], Alexander Düster [a,*], Wolfgang Bier [b],
Zohar Yosibash [c], Ernst Rank [a]

[a] *Lehrstuhl für Bauinformatik, Fakultät für Bauingenieur- und Vermessungswesen, Technische Universität München, Germany*
[b] *Institute of Mechanics, University of Kassel, Germany*
[c] *Pearlstone Center for Aeronautical Studies, Department of Mechanical Engineering, Ben-Gurion University of the Negev, Beer-Sheva, Israel*

Abstract

The simulation of powder compaction problems (die-compaction and cold isostatic pressing) is considered herein by an implicit high-order (*p*-version) finite element method. In this class of problems use is made of a finite strain viscoplasticity model with evolution equations for internal variables developed for the highly compressible behavior in powder compaction processes. The classical approach of implicit finite elements applies the combination of Backward-Euler integration scheme and the Multilevel-Newton algorithm to solve the system of differential-algebraic equations resulting from the space-discretized weak formulation by means of *p*-version finite elements. This approach requires on Gauss-point level a robust stress-algorithm. The challenging investigations are the incorporation of the applied highly non-linear viscoplasticity model into a *p*-version finite element formulation using follower load applications. Several axisymmetric numerical examples show the feasibility and good performance of this *p*-version approach.
© 2007 Elsevier B.V. All rights reserved.

Keywords: *p*-Version FEM; Finite strain; Viscoplasticity; Axisymmetry; Die-compaction; Cold isostatic pressing; Metal powder compaction

1. Introduction

Powder compaction and powder metallurgic products are used in a wide range of industries, from aerospace, medical and automotive applications to household appliances. Examples are turbine blades, prosthetic devices, pharmaceutical tablets, insulators, or tableware to name just a few. Numerical simulation of these processes provides the possibility to identify and solve problems already in the design stage and to adjust process parameters before investing in tools, equipment and trial and error studies. To the best of our knowledge this is the first paper addressing the use of a finite strain viscoplastic constitutive model with internal variables, which has been developed to represent compaction processes, in a high-order implicit finite element framework.

Often components produced by powder compaction are sintered after pressing, however, here we are only interested in describing the pressing process (die-compaction, cold isostatic pressing) under nearly isothermal conditions close to ambient temperatures (for the consideration of temperature during compaction, see for example [27]). One approach of describing the hardening behavior of powder during compaction applies yield-function based plasticity models. Most constitutive models published use yield functions of Drucker–Prager, Mohr–Coulomb or exponential function type (see references collected in [7]). We use a model extended in [18] to rate-dependent plasticity using a unique, convex single-surface yield function in stress space that can be applied to a number of pressure dependent materials. The constitutive model is based on the multiplicative decomposition of the deformation gradient into an elastic and a viscous part, where the dominating inelastic part evolves according to an associated flow rule of the inelastic strain-rate tensor relative to the inelastic interme-

* Corresponding author. Tel.: +49 89 289 25060; fax: +49 89 289 25051.
E-mail address: duester@bv.tum.de (A. Düster).

diate configuration and further evolution equations controlling the hardening behavior of the drop-like single-surface yield function. A particular problem of the stress computations of this class of pressure-dependent plasticity models is presented in [18] which is based on a proposal of Armero and Perez-Foguet [2], i.e. Perez-Foguet and Armero [28].

The paper is structured as follows: first the constitutive model is summarized. Then, the governing equations and the discretization by the *p*-version of the finite element method is presented. A brief survey of previous applications of high-order finite elements to geometric and material nonlinear problems is given. Finally, numerical examples demonstrate the feasibility of the large-strain implicit *p*-version approach with inelastic hardening to die-compaction and cold isostatic pressing processes. We compare the simulation of a complex process to experimental data and report good agreement with this validation example.

2. Kinematic and constitutive relations

To recap the constitutive relations of the rate-dependent finite strain plasticity model, the kinematic relations are first summarized. The constitutive model proposed in [7] is based on the multiplicative decomposition of the deformation gradient $\mathbf{F} = \text{Grad } \vec{\chi}_R(\vec{X}, t)$,

$$\mathbf{F} = \widehat{\mathbf{F}}_e \mathbf{F}_v, \qquad \det \mathbf{F} > 0, \quad \det \widehat{\mathbf{F}}_e > 0, \quad \det \mathbf{F}_v > 0 \qquad (1)$$

with the motion $\vec{x} = \vec{\chi}_R(\vec{X}, t)$ of a material point $\vec{X}$ at time t. $\widehat{\mathbf{F}}_e$ defines the elastic and $\mathbf{F}_v$ the inelastic part inducing the so-called inelastic intermediate configuration. A fictitious unloading leads to the inelastic Green strain tensor $\mathbf{E}_v = 1/2(\mathbf{F}_v^T \mathbf{F}_v - \mathbf{I})$, where $\mathbf{E} = 1/2(\mathbf{F}^T \mathbf{F} - \mathbf{I})$ defines the Green strain tensor of the total deformation. The elastic strains are obtained by the difference $\mathbf{E}_e = \mathbf{E} - \mathbf{E}_v$, $\mathbf{E}_e = 1/2(\mathbf{F}^T \mathbf{F} - \mathbf{F}_v^T \mathbf{F}_v)$. The push-forward operation of the strain-like tensorial variables relative to the reference configuration into quantities relative to the inelastic intermediate configuration reads

$$\widehat{\mathbf{\Gamma}} = \mathbf{F}_v^{-T} \mathbf{E} \mathbf{F}_v^{-1}, \quad \widehat{\mathbf{\Gamma}}_e = \mathbf{F}_v^{-T} \mathbf{E}_e \mathbf{F}_v^{-1}, \quad \widehat{\mathbf{\Gamma}}_v = \mathbf{F}_v^{-T} \mathbf{E}_v \mathbf{F}_v^{-1} \qquad (2)$$

leading to

$$\widehat{\mathbf{\Gamma}} = \widehat{\mathbf{\Gamma}}_e + \widehat{\mathbf{\Gamma}}_v, \qquad (3)$$

$$\widehat{\mathbf{\Gamma}}_e = \frac{1}{2}\left(\widehat{\mathbf{F}}_e^T \widehat{\mathbf{F}}_e - \mathbf{I}\right), \qquad (4)$$

$$\widehat{\mathbf{\Gamma}}_v = \frac{1}{2}\left(\mathbf{I} - \mathbf{F}_v^{-T} \mathbf{F}_v^{-1}\right), \qquad (5)$$

whereas the transformation of the material time derivatives of the Lagrangean quantities, $\dot{\mathbf{E}} = \dot{\mathbf{E}}_e + \dot{\mathbf{E}}_v$,

$$\overset{\triangle}{\widehat{\mathbf{\Gamma}}} = \mathbf{F}_v^{-T} \dot{\mathbf{E}} \mathbf{F}_v^{-1}, \quad \overset{\triangle}{\widehat{\mathbf{\Gamma}}}_e = \mathbf{F}_v^{-T} \dot{\mathbf{E}}_e \mathbf{F}_v^{-1}, \quad \overset{\triangle}{\widehat{\mathbf{\Gamma}}}_v = \mathbf{F}_v^{-T} \dot{\mathbf{E}}_v \mathbf{F}_v^{-1} \qquad (6)$$

yield an additive decomposition

$$\overset{\triangle}{\widehat{\mathbf{\Gamma}}} = \overset{\triangle}{\widehat{\mathbf{\Gamma}}}_e + \overset{\triangle}{\widehat{\mathbf{\Gamma}}}_v = \dot{\widehat{\mathbf{\Gamma}}} + \mathbf{L}_v^T \widehat{\mathbf{\Gamma}} + \widehat{\mathbf{\Gamma}} \mathbf{L}_v, \qquad (7)$$

$$\overset{\triangle}{\widehat{\mathbf{\Gamma}}}_e = \dot{\widehat{\mathbf{\Gamma}}}_e + \mathbf{L}_v^T \widehat{\mathbf{\Gamma}}_e + \widehat{\mathbf{\Gamma}}_e \mathbf{L}_v, \qquad (8)$$

$$\overset{\triangle}{\widehat{\mathbf{\Gamma}}}_v = \mathbf{D}_v = \dot{\widehat{\mathbf{\Gamma}}}_v + \mathbf{L}_v^T \widehat{\mathbf{\Gamma}}_v + \widehat{\mathbf{\Gamma}}_v \mathbf{L}_v \qquad (9)$$

of Oldroyd-derivatives relative to the inelastic intermediate configuration, see, for example [19–21]. In Eqs. (7)–(9), the inelastic velocity gradient tensor $\mathbf{L}_v$ and its symmetric part $\mathbf{D}_v$

$$\mathbf{L}_v = \dot{\mathbf{F}}_v \mathbf{F}_v^{-1}, \qquad (10)$$

$$\mathbf{D}_v = \frac{1}{2}(\mathbf{L}_v + \mathbf{L}_v^T) \qquad (11)$$

are applied. Furthermore, the elastic and inelastic right Cauchy–Green tensors are defined

$$\widehat{\mathbf{C}}_e = \widehat{\mathbf{F}}_e^T \widehat{\mathbf{F}}_e, \quad \mathbf{C}_v = \mathbf{F}_v^T \mathbf{F}_v, \qquad (12)$$

for later use.

The strain measure (4) is purely elastic and the strain tensor (5) designates the strain rate (9), which is purely inelastic implying the motivation to make use of the quantities in the elasticity relation and the flow rule.

The elastic strain defines the stress state in the intermediate configuration

$$\widehat{\mathbf{T}} = (\Lambda \ln J_e - \mu)\widehat{\mathbf{C}}_e^{-1} + \mu \mathbf{I}, \qquad (13)$$

where a Simo&Pister type model is applied, see [31]. $J_e = \det \widehat{\mathbf{F}}_e = (\det \widehat{\mathbf{C}}_e)^{1/2}$ defines the elastic part of the volumetric deformation. The stress tensor relative to the inelastic intermediate configuration $\widehat{\mathbf{T}}$ is related to the 2nd Piola–Kirchhoff tensor $\widetilde{\mathbf{T}}$ and the weighted Cauchy stress tensor $\mathbf{S}$ (Kirchhoff stress tensor) by the push-forward and pull-back operations

$$\widehat{\mathbf{T}} = \mathbf{F}_v \widetilde{\mathbf{T}} \mathbf{F}_v^T = \widehat{\mathbf{F}}_e^{-1} \mathbf{S} \widehat{\mathbf{F}}_e^{-T} \qquad (14)$$

respectively, with $\mathbf{S} = (\det \mathbf{F})\mathbf{T}$, where $\mathbf{T}$ defines the Cauchy stress tensor. In view of a thermomechanical consistent constitutive model, the Mandel stress tensor $\widehat{\mathbf{P}} = \widehat{\mathbf{C}}_e \widehat{\mathbf{T}}$ is introduced controlling the evolution of the inelastic flow

$$\overset{\triangle}{\widehat{\mathbf{\Gamma}}}_v = \lambda \frac{\partial F}{\partial \widehat{\mathbf{P}}} = \lambda \left(\frac{\partial F}{\partial \mathbf{I}_1} \mathbf{I} + \frac{\partial F}{\partial \mathbf{J}_2} \widehat{\mathbf{P}}^D\right), \qquad (15)$$

for more details see [7]. F is the yield surface defined in (19), $\mathbf{I}_1 = \text{tr } \widehat{\mathbf{P}}$ and $\mathbf{J}_2 = 1/2\widehat{\mathbf{P}}^D \cdot \widehat{\mathbf{P}}^D$ define the invariants of the Mandel stress tensor. $\text{tr } \mathbf{A} = a_k^k$ symbolizes the trace of a tensor, $\mathbf{A} \cdot \mathbf{B} = a_i^j b_j^i$ the inner product of two second order tensors and $\mathbf{A}^D = \mathbf{A} - 1/3(\text{tr } \mathbf{A})\mathbf{I}$ the deviator operator.

$$\lambda = \frac{1}{\eta} \left\langle \frac{F}{\sigma_0} \right\rangle^{r_v} \qquad (16)$$

is a constitutive function expressing the case distinction into elastic and inelastic deformations, where $\langle x \rangle =$

$(x + |x|)/2$ defines the Macauley-brackets, i.e. $\langle x \rangle = 0$ for $x \leqslant 0$ and $\langle x \rangle = x$ for $x > 0$.

The main ingredients of the model are the yield function and its evolution during the compaction process. There are a number of yield function based plasticity models in the literature (see [7] and the references therein). However, the application of Drucker–Prager type models with caps to reproduce the hardening behavior in the compressive range imply non-differentiable yield surfaces and, accordingly, require particular numerical techniques to solve the problem arising at the edges. The application of single surface models like those of [4,8,13] pose the difficulty to guarantee the convexity during the evolution or to properly account for the non-uniqueness of additionally occurring regions in the stress-space. To this end the new convex single surface yield function concept discussed in [7] is applied. This yield surface is generated by interpolating an ellipsoidal function

$$g_1(\mathbf{I}_1, \sqrt{\mathbf{J}_2}) = \sqrt{\mathbf{J}_2 + \alpha(\mathbf{I}_1 - 3\xi)^2} - k \qquad (17)$$

and an exponential function

$$g_2(\mathbf{I}_1, \sqrt{\mathbf{J}_2}) = \sqrt{\mathbf{J}_2 + \delta} - k + A_1 e^{A_2 I_1} \qquad (18)$$

using an interpolation formula of [26,3],

$$F(\mathbf{I}_1, \sqrt{\mathbf{J}_2}) = ck \ln \left(\frac{e^{g_1(\mathbf{I}_1, \sqrt{\mathbf{J}_2})/(ck)} + e^{g_2(\mathbf{I}_1, \sqrt{\mathbf{J}_2})/(ck)}}{2} \right). \qquad (19)$$

The abbreviations

$$k = \sqrt{\alpha(I_0 - 3\xi)^2}, \quad A_1 = \frac{k}{(1 - \sqrt{1 - r^2})^{I_0/((3\xi - I_0)(1+r))}},$$
$$A_2 = \ln(k/A_1)/I_0 \qquad (20)$$

are introduced. For a schematic representation of F we refer to Fig. 1. The parameter c controls the closeness of the resulting function to the lower one of both functions so that the resulting function has the tear-drop like form.
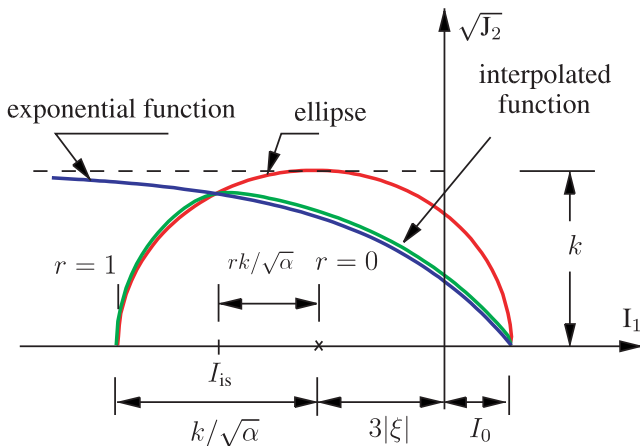
The internal variable ξ controls the hardening in the direction of the hydrostatic stress state and α influences the form of the drop-like yield function containing the parameters I_0, r and c which are defined in advance. The small quantity δ has been introduced to avoid a vertex singularity at the intersection of the yield function with the hydrostatic axis close to I_0 following a proposal of [1]. I_0 is a fixed right bound in our approach.

The volumetric inelastic deformation $\det \mathbf{F}_v$, or $\det \mathbf{C}_v$, is related to the center of the yield function defined by

$$\xi(r_K) = a_1 r_K + a_2 r_K^3 - \frac{a_3}{r_K - r_{K0}} - \frac{a_3}{r_{K0}}, \qquad (21)$$

see proposal in Szanto et al. [35], depending on the strain-like internal variable

$$r_K = \hat{r}_K(\mathbf{C}_v) = \ln(\det \mathbf{C}_v)/2 \rightarrow \dot{r}_K = \operatorname{tr} \overset{\triangle}{\hat{\mathbf{\Gamma}}}_v = \operatorname{tr} \mathbf{L}_v. \qquad (22)$$

a_1, a_2, a_3 and r_{K0} are material parameters. ξ defines the center of the ellipsoid and is obviously related to plastic volumetric deformation and, therefore, to the relative density of the material. The internal variable α describes the "deviatoric behavior" and evolves according to

$$\dot{\alpha} = \lambda \left(\frac{c_D}{\alpha} (\widehat{\mathbf{P}} - \xi \mathbf{I}) \cdot \frac{\partial F}{\partial \widehat{\mathbf{P}}} - \alpha b_D \chi \right), \qquad (23)$$

with the abbreviation

$$\chi = \hat{\chi}(\mathbf{I}_1, \mathbf{J}_2, \xi, \alpha) = \sqrt{3 \left(\frac{\partial F}{\partial \mathbf{I}_1} \right)^2 + 2 \mathbf{J}_2 \left(\frac{\partial F}{\partial \mathbf{J}_2} \right)^2}. \qquad (24)$$

b_D and c_D are material parameters. The process of identifying the material parameters is presented in [6] and the resulted values for a copper powder are recapped in Table 1. Because the applied numerical scheme is based on the Total-Lagrangean formulation, the quantities relative to the reference configuration are required. In Table. 2 the model is compiled indicating that in three dimensions 7 evolution equations have to be integrated, which are subject to a case distinction called loading condition (six equations due to $\mathbf{C}_v$ and one for α).

3. Governing equations and discretization with the *p*-version of the finite element method

For the spatial discretization the *p*-version of the finite element method is applied. Hierarchic Ansatz spaces are created using the tensor product of integrated Legendre polynomials. This construction also provides the possibility to use different polynomial degrees in each spatial direction (anisotropic Ansatz spaces). As generally a coarse mesh compared to *h*-version calculations is used, a precise description of curved boundaries is essential. This is achieved by the blending function method [15] without increasing the number of elements. The *p*-version, contrary to the classical *h*-version, keeps the mesh fixed and achieves convergence by raising the polynomial degree *p* of the Ansatz functions. For elliptic problems (i.e. linear elastic-

Fig. 1. Yield function concept of interpolating simple convex models proposed by Bier and Hartmann [7].

Table 1
Material parameters (initial condition: $\alpha(0) = 0.558$)

Identified material parameters							Specified parameters					
Λ (GPa)	μ (GPa)	a_1 (MPa)	a_2 (MPa)	a_3 (MPa)	r_{K0} (MPa^{-1})	b_D (MPa^{-1})	c_D (–)	r_v (–)	r (–)	c (MPa^2)	I_0 (MPa^2)	δ (MPa)	σ_0
5.2	8.3	24.8	23.6	15.9	-0.87	2.68	10^{-4}	1	0.3	0.01	1	0.1	1

Table 2
Constitutive model expressed with quantities relative to the reference configuration

	Elasticity	Viscoplasticity
Loading condition	$F \leqslant 0$	$F > 0$
Elasticity relation	$\widetilde{\mathbf{T}} = (\Lambda \ln J_e - \mu)\mathbf{C}^{-1} + \mu\mathbf{C}_v^{-1}$	
Flow rule	$\dot{\mathbf{C}}_v = \mathbf{0}$	$\dot{\mathbf{C}}_v = \lambda 2(\frac{\partial F}{\partial I_1}\mathbf{I} + \frac{\partial F}{\partial J_2}(\mathbf{C}\widetilde{\mathbf{T}} - (I_1/3)\mathbf{I}))\mathbf{C}_v$
Distortional hardening	$\dot{\alpha} = 0$	$\dot{\alpha} = \lambda(\frac{c_D}{\alpha}((I_1 - 3\xi)\frac{\partial F}{\partial I_1} + \sqrt{J_2}\frac{\partial F}{\partial\sqrt{J_2}}) - b_D\alpha\chi)$
Abbrev.	$I_1 = \text{tr}(\widetilde{\mathbf{T}}\mathbf{C})$, $J_2 = (\mathbf{C}\widetilde{\mathbf{T}} \cdot \widetilde{\mathbf{T}}\mathbf{C} - I_1^2/3)/2$, $J_e = ((\det\mathbf{C})/(\det\mathbf{C}_v))^{1/2}$	
	$r_K = \ln(\det\mathbf{C}_v)/2$, $\xi = a_1 r_K + a_2 r_K^3 - \frac{a_3}{r_K - r_{K0}}$, $\lambda = \frac{1}{\eta}(F/\sigma_0)^{r_v}$	

ity) this method and its benefits are summarized in the monograph of Szabó and Babuška [33]. The *p*-version is accepted as an efficient approach for linear and geometrically nonlinear problems [25] but little work has been carried out for physically nonlinear applications. Small strain elastoplasticity with the *p*-version was investigated by Szabo et al. [32], Holzer and Yosibash [23], Jeremic and Xenophontos [24]. Düster and Rank compared the *p*-version to an adaptive *h*-version [11] for the deformation theory of plasticity. The high-order approach for the small strain J_2-flow theory of plasticity was studied in [12]. The *p*-version is robust also to severe element distortion and large aspect ratios. Locking is overcome by raising the polynomial degree. This property, well established for small strain elastic problems (for a comprehensive discussion we refer to [33]), also carries over to finite strain hyperelasticity applications, particularly, to overcome volumetric locking effects for nearly incompressible material, [10,22,36]. The blending function method provides efficient means for the exact description of curved boundaries also in the nonlinear regime. Given the advantages of *p*-FE methods, it is natural to extend them to finite strain plasticity problems as follows.

In view of the numerical treatment of the initial boundary-value problem given by the local balance of linear momentum (under the assumption that inertia terms are neglected)

$$\text{Div}(\mathbf{F}\widetilde{\mathbf{T}}) + \rho_R\vec{k} = \vec{0} \tag{25}$$

and the stress-defining equations of Table 2, a finite element discretization in the sense of *p*-version finite elements is applied. To this end, the weak formulation (principle of virtual displacements) has to be exploited, which must be fulfilled at every time t

$$W(t, \vec{u}, \delta\vec{u}, \mathbf{q}) = W_{\text{int}} - W_{\text{ext}}$$

$$= \int_V \delta\mathbf{E} \cdot \widetilde{\mathbf{T}}(\mathbf{C}, \mathbf{q})\,\mathrm{d}V - W_{\text{ext}} = 0. \tag{26}$$

$\delta\mathbf{E} = 1/2(\mathbf{F}^T\delta\mathbf{H} + \delta\mathbf{H}^T\mathbf{F})$ symbolizes the virtual Green strain tensor ($\mathbf{F} = \mathbf{I} + \mathbf{H}$, $\mathbf{H} = \text{Grad }\vec{u}(\vec{X}, t)$, $\vec{u}$ represents the displacement field) with the gradient $\delta\mathbf{H} = \text{Grad }\delta\vec{u}(\vec{X})$ of the virtual displacements $\delta\vec{u}(\vec{X})$ and the vector $\mathbf{q}(\vec{X}, t)$ of the internal variables – viscous right Cauchy–Green tensor $\mathbf{C}_v$ and the axis ratio of the ellipsoidal-like yield-function α – introduced in Section 2. The virtual work of the external forces in Eq. (26) is given by

$$W_{\text{ext}}(t, \vec{u}, \delta\vec{u}) = \int_a \delta\vec{u}(\vec{x}) \cdot \vec{t}(\vec{x}, t)\,\mathrm{d}a + \int_V \delta\vec{u}(\vec{X}) \cdot \rho_R(\vec{X})\vec{k}\,\mathrm{d}V, \tag{27}$$

with the traction vector $\vec{t} = \mathbf{T}\vec{n}$ depending on the normal $\vec{n}$ to the surface element $\mathrm{d}a$ in the current configuration, $\mathbf{T}$ the Cauchy stress tensor, ρ_R the density in the reference configuration, and $\vec{k}$ the acceleration.

In order to solve the coupled Eqs. (26) and (27) and those of Table 2, use is made of the classical approach of semi-discretization. The application of the vertical method of lines states that in a first step the spatial discretization (domain discretization by introducing elements, here, in combination with the blending function method, introducing shape functions and applying spatial integration) has to be carried out yielding a system of non-linear equations [14],

$$\mathbf{g}(t, \mathbf{u}, \mathbf{q}) = \sum_{e=1}^{n_e} \mathbf{Z}^{eT} \sum_{j,k,l} w_{jkl}\widetilde{\mathbf{B}}_{jkl}^{eT}(\mathbf{u}(t))\underbrace{\widetilde{\mathbf{h}}(\mathbf{C}_{jkl}^e, \mathbf{q}_{jkl}^e)}_{\widetilde{\mathbf{T}}_{jkl}^e} \det\mathbf{J}_{jkl}^e$$

$$- \overline{\mathbf{p}}(t, \mathbf{u}) = \mathbf{0}, \tag{28}$$

where $\sum_{e=1}^{n_e} \mathbf{Z}^{eT}\{\ \}$ defines the assemblage operator of the internal force vector, $\widetilde{\mathbf{B}}_{jkl}^e$ the strain–displacement matrix in a *p*-version finite element e at Gauss-point ξ_{jkl}, $\mathbf{J}_{jkl}^e$ the Jacobian of the coordinate transformation related to reference element e at Gauss-point jkl, $\overline{\mathbf{p}}(\mathbf{u}, t)$ the prescribed, external, equivalent modal force vector which might depend on the deformation itself in the case of, for example, follower loads, $\mathbf{h}(\mathbf{C}, \mathbf{q})$ the elasticity relation composed in

Table 2, $\mathbf{u}$ the unknown modal displacement vector and $\mathbf{q}$ the vector of all internal variables $\mathbf{q}_{jkl}^e$ at all Gauss-points of all elements. n_e is the number of elements and w_{jkl} denotes the weighting factors of the spatial quadrature. This equation contains the stresses $\widehat{\mathbf{T}}_{jkl}^e$ which have to be computed at the spatial quadrature points namely the Gauss-points of the *p*-version finite elements. In other words, the internal variables, which occur in the stress-defining relation, are necessary to be evaluated at the spatial quadrature points. These are defined by evolution equations in the case of viscoplasticity, i.e. ordinary differential equations of first order, $\dot{\mathbf{q}} = \mathbf{r}(t, \mathbf{u}, \mathbf{q})$. All evolution equations at all spatial quadrature points form, together with the discretized weak formulation (28), a differential algebraic equation (DAE) system

$$\mathbf{F}(t, \mathbf{y}(t), \dot{\mathbf{y}}(t)) := \left\{ \begin{array}{c} \mathbf{g}(t, \mathbf{u}(t), \mathbf{q}(t)) \\ \dot{\mathbf{q}}(t) - \mathbf{r}(t, \mathbf{u}(t), \mathbf{q}(t)) \end{array} \right\} = \mathbf{0}, \qquad (29)$$

with

$$\mathbf{y}(t) := \left\{ \begin{array}{c} \mathbf{u}(t) \\ \mathbf{q}(t) \end{array} \right\}, \quad \text{and the initial conditions}$$

$$\mathbf{y}(t_0) := \left\{ \begin{array}{c} \mathbf{u}(t_0) \\ \mathbf{q}(t_0) \end{array} \right\} = \left\{ \begin{array}{c} \mathbf{u}_0 \\ \mathbf{q}_0 \end{array} \right\} =: \mathbf{y}_0. \qquad (30)$$

If the traction term in (27) depends on the deformation as in the case of pressure loads, $\vec{t} = \vec{t}(\vec{u}, t)$, the deformation-dependence, which is an essential issue in powder compaction applications, has to be considered specifically in the numerical treatment (in this respect, we refer to [22,36] and the literature cited therein).

To summarize, the algebraic part is the result of the discretized weak formulation and the differential part is the outcome of the constitutive model's ordinary differential equations occurring at all spatial integration points. The subsequent step of the vertical method of lines defines the temporal discretization. If the DAE-system (29) is solved by means of a Backward-Euler method a coupled system of non-linear equations results at each time t_{n+1}

$$\left\{ \begin{array}{c} \mathbf{G}_{n+1}(\mathbf{u}_{n+1}, \mathbf{q}_{n+1}) \\ \mathbf{L}_{n+1}(\mathbf{u}_{n+1}, \mathbf{q}_{n+1}) \end{array} \right\} := \left\{ \begin{array}{c} \mathbf{g}(t_{n+1}, \mathbf{u}_{n+1}, \mathbf{q}_{n+1}) \\ \mathbf{l}(t_{n+1}, \mathbf{u}_{n+1}, \mathbf{q}_{n+1}) \end{array} \right\} = \mathbf{0}, \qquad (31)$$

with

$$\mathbf{l}(t_{n+1}, \mathbf{u}_{n+1}, \mathbf{q}_{n+1}) = \mathbf{q}_{n+1} - \mathbf{q}_n - \Delta t_n \mathbf{r}(t_{n+1}, \mathbf{u}_{n+1}, \mathbf{q}_{n+1}). \qquad (32)$$

The explicit dependence of the time t is the result of the prescribed Neumann and Dirichlet boundary conditions. It must be emphasized that the internal variables and their evolution equations are only formally assembled to $\mathbf{q}_{n+1}$. However, all equations in $\mathbf{L}_{n+1}$ are block-wise (Gauss-point wise) decoupled so that at each Gauss-point a Backward-Euler step can be carried out.

In this algorithm the local integration step, see also Eq. (32), has to be conducted at each Gauss-point inside the global iteration step (m) of the Multilevel-Newton algorithm for given element displacements, see [17]. In other words, on Gauss-point level the non-linear system

$$\widetilde{\mathbf{L}}(\mathbf{q}_{n+1}^{(m)}) = \mathbf{q}_{n+1}^{(m)} - \mathbf{q}_n^{(m)} - \lambda_{n+1}^{(m)} \Delta t_n \mathbf{r}(\mathbf{q}_{n+1}^{(m)}) = \mathbf{0} \qquad (33)$$

in the case of inelastic loading ($F > 0$) with

$$\lambda_{n+1}^{(m)} = \frac{1}{\eta} \left(\frac{F(\mathbf{q}_{n+1}^{(m)})}{\sigma_0} \right)^{r_v} \qquad (34)$$

has to be solved (here, the elastic-predictor – plastic-corrector scheme is exploited for incorporating the case distinctions in Table 2). Eq. (33) represents a system of seven non-linear equations. In order to take into account the rate-independent sub-problem, the "plastic multiplier" (34) times the stepsize Δt_n can be substituted by a new variable, $\zeta_{n+1}^{(m)} := \lambda_{n+1}^{(m)} \Delta t_n$, so that an additional scalar equation is obtained representing the yield condition in the case of rate-independent elastoplasticity (for $\eta = 0$, $r_v = 1$, and $\sigma_0 = 1$):

$$\mathbf{L}(\mathbf{q}_{n+1}^{(m)}, \zeta_{n+1}^{(m)}) = \left\{ \begin{array}{c} \mathbf{q}_{n+1}^{(m)} - \mathbf{q}_n^{(m)} - \zeta_{n+1}^{(m)} \mathbf{r}(\mathbf{q}_{n+1}^{(m)}) \\ F^{r_v}(\mathbf{q}_{n+1}^{(m)}) - \zeta_{n+1}^{(m)} \sigma_0^{r_v} \frac{\eta}{\Delta t_n} \end{array} \right\} = \mathbf{0}. \qquad (35)$$

Frequently, a classical Newton–Raphson method is applied for solving the local system (35). However, this fails in most situations for compression dependent yield functions, see [18,2,28] and the literature cited therein. Thus, a line-search procedure combined with inequality constraints is formulated in order to stabilize the local iteration procedure.

The effect of numerical quadrature in the *p*-version is discussed in [5]. The error introduced by the integration scheme should not exceed the discretization error and decay as fast as the discretization error. For smooth problems it is sufficient to choose $p + 1$ integration points in each spatial direction. If this condition is violated overintegration may be necessary depending of the non-smoothness of the problem. For the geometrically and physically non-linear problems investigated here the integration order is mentioned for the different examples, most times we use $p + 3$.

4. Numerical results

In this section we present numerical results applying the constitutive relations of finite strain viscoplasticity as described in Section 2 to an implicit *p*-version implementation of the finite element method described in the previous section. Computation times when reported refer to an Opteron processor with 2.4 GHz. The applied material parameters are summarized in Table 1.

Failure can occur both on the global and local level of the applied Multilevel-Newton algorithm. It is possible that the local stress algorithm (Backward-Euler step for computing the internal variables) does not converge in solving the local nonlinear equations (35) to determine the stresses for a given state of displacements. It is also possible that the global iterations fail to meet the convergence criterion. In both cases the stepsize is reduced and the step is repeated. In the beginning of a compression process of loose powder the stepsize has to be chosen small. The

inelastic deformations for small loading result in quite large displacements in the beginning. As the material consolidates the stepsize can be increased. For efficient calculations it is vital that an adaptive stepsize control is implemented and the stepsize is increased when possible. Experience revealed that the number of global iterations can not be used as single criterion to choose the stepsize due to the possibility of sudden local failure (i.e. the stress algorithm does not converge). It proved sufficient to implement a heuristic approach: if the global residuum or the displacement increment $\Delta\mathbf{u}$ increases in e.g. five successive iterations the stepsize is decreased. If the maximum or almost the maximum of allowed global iterations was needed for global convergence the stepsize is not changed. In all successful other cases the stepsize is increased (e.g. by the factor $\phi_{inc} = 1.2$) until the prescribed maximum stepsize is reached. If local or global failure occurs the stepsize is decreased (by the factor $\phi_{dec} = 0.7$) and the step is repeated.

The resulting element and global stiffness matrices are unsymmetric because of the consistent linearization (application of implicit function theorem within the Multi-level-Newton algorithm). Thus, the general sparse solver umfpack [9] is applied that allows to use optimized BLAS-routines for basic linear algebra operations.

To check calculations for plausibility it is helpful to verify the global equilibrium. The reaction forces corresponding to certain degrees of freedom are the entries of the assembled internal force vector. For details we refer to [16]. Using the *p*-version with a hierarchic basis only those degrees of freedom corresponding to the nodal (i.e. linear) modes have to be taken into account. The reason is that contrary to the classical Lagrange basis we use integrated Legendre polynomials where the sum of all the shape functions over an edge is not equal to unity, however the nodal modes fulfill this criterion.

4.1. Die-compaction examples

4.1.1. Cylinder

A cylinder made of copper powder with initial relative density of $\rho_{rel0} = \rho_R/\rho_0 = 0.42$ is compacted under displacement control. The reference density ρ_0 is the density of solid copper while ρ_R is the density of the powder body in the initial state. Exploiting the radial symmetry we use axisymmetric elements, see Fig. 2 for the system and the boundary conditions. This example is analogous to the die-compaction experiments that were conducted to determine the parameters of the constitutive model in [6]. Due to the homogenous deformation, i.e. the deformation gradient is the same for all points of the body, one element with linear Ansatz functions is sufficient. The current relative density ρ/ρ_0 is calculated by dividing the initial relative density $\rho_{rel0} = 0.42$ by the determinant of the deformation gradient $\rho/\rho_0 = 0.42/\det\mathbf{F}$.

This example serves mainly to verify the proper implementation of the stress algorithm including unloading
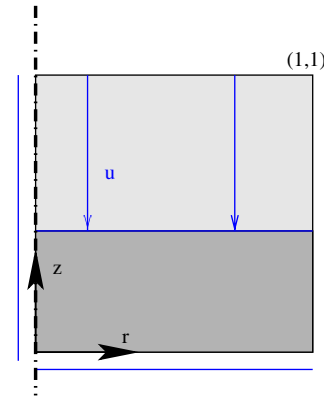
Fig. 2. System and boundary conditions for the die-compaction example with displacement control.

and reloading. At the end of a partial run the current state is written to the mesh file storing the element displacement vectors and the internal variables at all integration points. In the restart procedure these quantities are read and used e.g. to compute the tangential stiffness matrix for the next iteration. This restart feature is necessary for more complex processes as described in Section 4.2.2. Fig. 3 displays the evolution of the axial and radial Cauchy stress vs. the relative density. It can be seen that
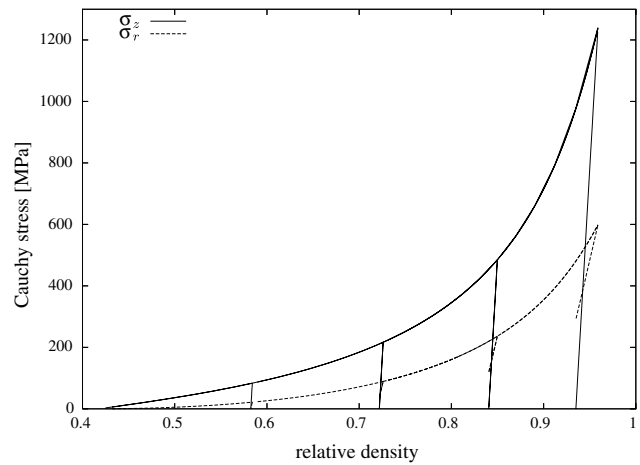
Fig. 3. Axial stress σ_z and radial stress σ_r vs. relative density ρ/ρ_0.
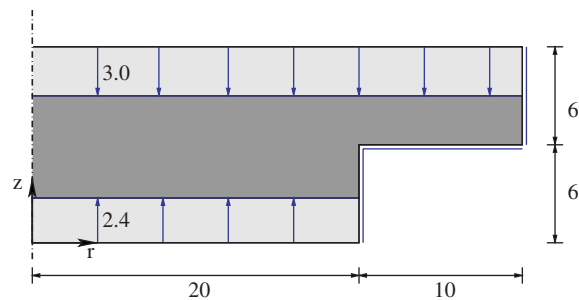
Fig. 4. System and boundary conditions for the L-shape example with displacement control.

the reloading follows exactly the elastic unloading path. As the sample is clamped in radial direction, an unloading in axial direction decreases the axial stress σ_z to zero while there remain radial stresses due to the boundary conditions.

4.1.2. L-shaped domain

The second example is a rotationally symmetric structure with L-shaped cross section. Axisymmetric elements are used to discretize the system shown in Fig. 4. Displacement controlled pressing at the top and bottom introduces an inhomogeneous deformation ($\bar{u}_{\text{bottom}} = 2.4 = -0.8\bar{u}_{\text{top}}$), cf. Fig. 5. The reentrant corner allows to study the influence of a singularity.

The deformed body is depicted in Fig. 5 and the distribution of the relative density is shown in Fig. 6.

It is well known for *linear* problems with corner singularities how to construct a suitable mesh for the *p*-version of the finite element method [33]. The same mesh layout is applied for this geometric and material nonlinear problem. We compare the *p*-version approach where the polynomial degree of the hierarchic Ansatz functions is raised on a fixed mesh graded once towards the reentrant corner with a geometric progression factor of 0.15 shown in Fig. 7a (referred as 'graded mesh') to meshes with a uniform subdivision of the base elements and fixed low polynomial degree as shown in Fig. 7b. This uniform *h*-refinement subdivides each of the five elements of the base mesh in up to 41×41 sub-elements ('*h*-meshes'), Fig. 7c shows an example where each base element is divided in 15×15 elements.

Elastoplastic ($\eta = 0$) and viscoplastic investigations ($\eta > 0$) were carried out for both mesh layouts to study the convergence in terms of stresses. As a constitutive model with internal variables is employed the stresses are initially only available at the Gauss points. To be able to extract the stress at the point $r = 5$, $z = 9$ for all used meshes without further processing, an odd number of Gauss–Legendre points is chosen resulting in an integration order in each spatial direction of $p \geqslant 2$. Details are given when the different extension strategies are discussed.

The number of degrees of freedom is increased on the graded mesh by raising the polynomial degree of the Ansatz functions while on the *h*-meshes uniform subdivision of elements was done and a moderate polynomial degree $p = 2$ and $p = 3$ was used.
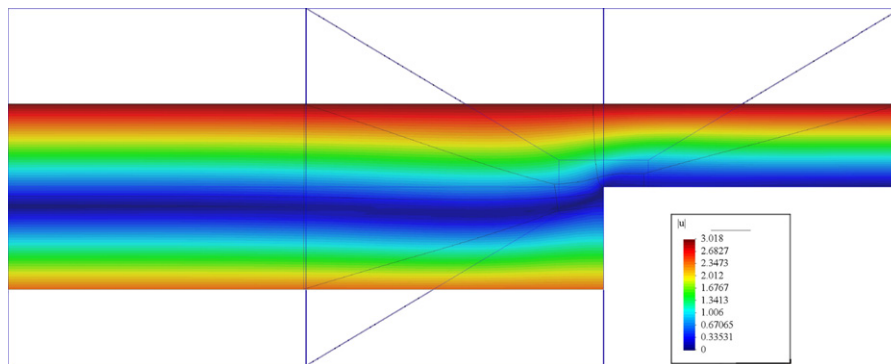
Fig. 5. Inhomogeneous deformation, shown is $|u|$. The background mesh depicts the undeformed configuration.
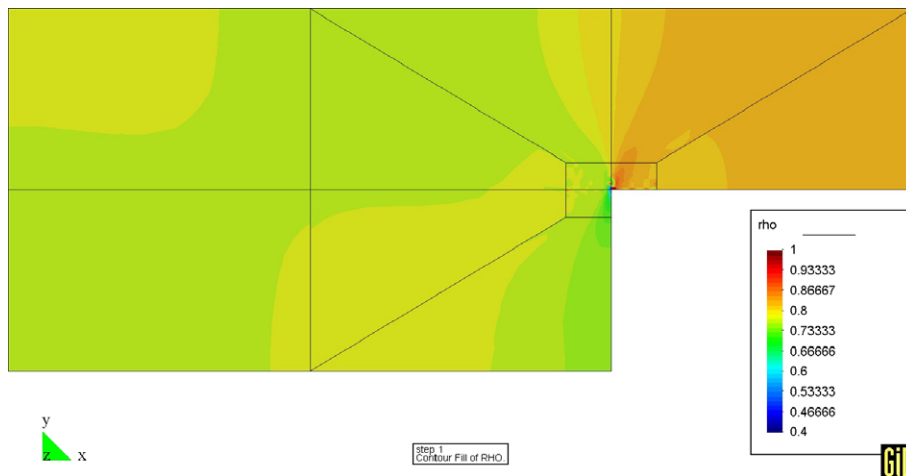
Fig. 6. Spatial distribution of the relative density mapped on the reference configuration. The mesh is refined once towards the singularity with the geometric progression factor 0.15. The polynomial degree of the shape functions is $p = 9$ on all elements.
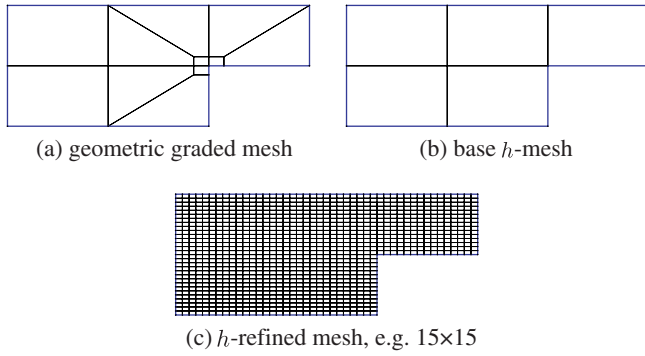
Fig. 7. The two classes of meshes employed. A geometrically graded mesh towards the singularity is used for *p*-extension while for *h*-extension with a fixed polynomial degree each element of the base *h*-mesh is uniformly subdivided in up to 41 × 41 elements: (a) geometric graded mesh; (b) base *h*-mesh; (c) *h*-refined mesh, e.g. 15 × 15.

For elastoplasticity ($\eta = 0$) we found that the *h*-refinement approach comes to the limit when the mesh is very fine. For $p = 2$ and an integration order of $p + 3 = 5$ the stress algorithm is not able to find a solution to the local nonlinear equation system for some integration points very close to the singularity. The global stepsize is consequently reduced over and over to a level that rendered calculations infeasible. This point was reached when during the *h*-refinement process[1] each base element was divided in 35×35 subelements, corresponding to 6125 elements and about 49.000 degrees of freedom with $p = 2$.

Therefore, the viscoplastic formulation was chosen with a small viscosity, $\eta = 1$. The effecting regularization is investigated in [18] and it is demonstrated there that a small viscosity did not alter the resulting stresses significantly. To rule out any effects of rate-dependence and to compare only the different spatial discretization strategies the following calculations were performed with a *fixed* small stepsize of 1/150 of the total displacement (in order to exclude any influence of the time- or load load-step control technique) and the order of Gauss integration set to 5 for the *h*-refinement[2] with $p = 2$ and $p = 3$. For *p*-refinement on the geometrically graded mesh the Gauss order is set to $p + 3$ for even *p*, e.g. if $p = 4$ we use an integration order of 7, and $p + 4$ for odd polynomial degrees of the Ansatz functions.

We investigate the convergence of the axial Cauchy stress σ_{zz} at the material point $r = 5$, $z = 9$. The stresses are plotted vs. the logarithm of the degrees of freedom in Fig. 8 comparing the different discretization strategies. The same data is shown in Fig. 9 where the abscissa shows the CPU-time in logarithmic scale. If instead of the computation time the total number of unknowns, i.e. displace-

---

[1] For the elastoplastic *h*-refinement with $\eta = 0$ each of the five base elements is subdivided in $n \times n$ elements, with $n = \{1, 3, 5, 7, 9, 11, 13, 15, 25, 27, 29, 31, 33, 35\}$.

[2] For the viscoplastic *h*-refinement with $\eta = 1$ each base element was subdivided in $n \times n$ elements, for $p = 2$ and $p = 3$ the same subdivisions were used with $n = \{1, 3, 5, 7, 9, 11, 13, 15, 25, 29, 35, 41\}$.
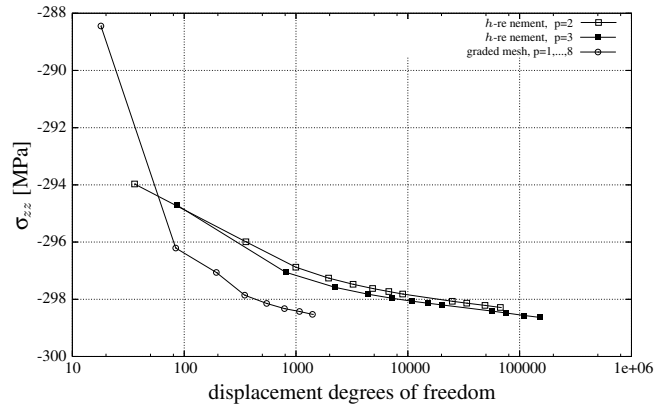
Fig. 8. Convergence of Cauchy-Stress σ_{zz} at point $r = 5$, $z = 9$ for the *h*- and *p*-refinement strategies in terms of the displacement degrees of freedom.
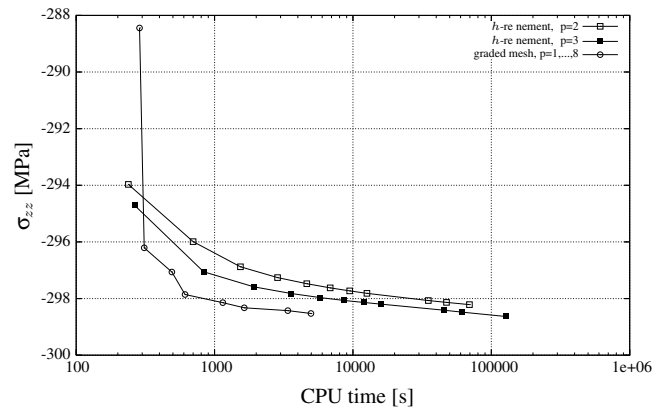
Fig. 9. Convergence of Cauchy-Stress σ_{zz} at point $r = 5$, $z = 9$ for the *h*- and *p*-refinement strategies vs. the CPU-time of the computation.

ment degrees of freedom plus internal variables (seven at each Gauss point), is plotted, Fig. 10, it is apparent that an investment in the polynomial order pays off. As for the *h*-refinement with $p = 2$ and $p = 3$ in both cases an integration order of 5 is used those curves are almost parallel as the number of internal variables that dominate the total
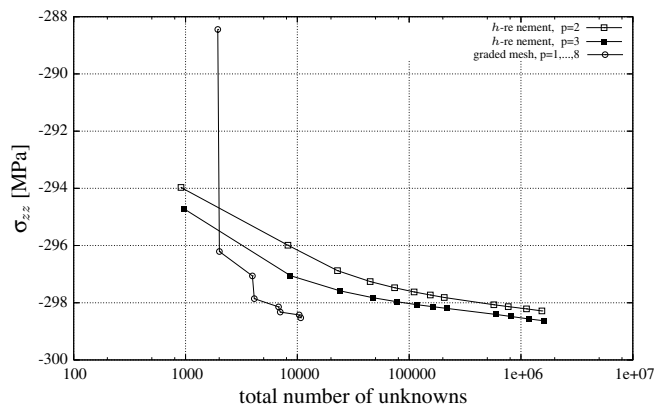
Fig. 10. Convergence of Cauchy-Stress σ_{zz} at point $r = 5$, $z = 9$ for the *h*- and *p*-refinement strategies vs. the total number of unknowns.

number of unknowns is the same, the minimal shift is due to the displacement degrees of freedom. The step-like descent of the p-extension is caused by the construction of the integration orders to be $p + 4$ for odd polynomial orders and $p + 3$ for even p. Consequently both $p = 5$ and $p = 6$ are integrated with order 9 for example.

From these plots it is apparent that for this nonlinear example the p-extension on the geometrically refined mesh needs significantly less degrees of freedom than the uniform h-refinement to achieve the same accuracy. This is also reflected in terms of computation time. The computational cost to set up the stiffness matrix of an element with a high polynomial degree is higher but due to the better rate of convergence of the p-extension this investment pays off also for finite strain applications with strongly nonlinear material like in this example.

The global equilibrium was checked by computing the out of balance force. To this end the reaction forces in axial direction along all boundary edges were added. The absolute residuum is below 10^{-5} N and the relative value (residuum over reaction force along top edge) for the reported runs is well below 10^{-8}.

4.2. Cold isostatic pressing

4.2.1. Sphere

To show the performance of an implicit p-version approach for a 'smooth' finite deformation problem the cold isostatic pressing of a ball made of copper powder is modeled. Exploiting the rotational symmetry only a quarter in the longitudinal plane of the sphere is meshed with axisymmetric elements. The pressure acts on the current surface, hence follower loading needs to be applied. The global implicit formulation using the Multilevel-Newton algorithm to solve the nonlinear equation system has the benefit that after an initial densification of the powder the stepsize can be increased resulting in short computation times compared to an explicit approach. Table 3 reports the computation time, number of displacement degrees of freedom and total number of unknowns for raising the polynomial degree p of the Ansatz functions on the fixed seven element mesh. As for the elastoplastic case ($\eta = 0$) 8 unknowns, cf. Eq. (35), have to be determined at each

quadrature point from a local nonlinear equation system, the number of displacement degrees of freedom must be augmented by all the internal variables of the complete structure to obtain the total number of unknowns for a meaningful criterion of the problem size as given in the last column of Table 3. It must be emphasized that the stress algorithm is given in a three-dimensional formulation. An adaption to the axisymmetric case, where only 5 internal variables are required, has not been carried out.

To obtain accurate results for the coarse mesh shown in Fig. 11 the circular arc is described analytically with the blending function method. We show the deformation after springback when the pressure of 500 MPa is released.

As the displacement $u := |\vec{u}|$ along the arc should be constant the influence of integration order and polynomial degree on the displacement can be investigated. Preliminary studies showed that for this problem it is enough to choose the order of Gauss–Legendre integration to be $p + 1$ in each spatial direction. For the chosen mesh with seven elements Fig. 12 shows on a logarithmic scale the deviation $|u - u_{\mathrm{ref}}|$ for $p = 3, 4, 5, 6$ along the circular arc after compression. The reference value $u_{\mathrm{ref}} = 1.16706829500301$ is the mean value of 800 sample points calculated from an overkill solution with 93 elements and $p = 10$. The arcs that are visible in the plot stem from the fact that the circular boundary is composed of four elements. The displacement field on each element is approximated by Ansatz functions of a certain degree. As only C^0 continuity over the element boundaries is prescribed, we see the peaks where two elements meet. From Fig. 12 we can conclude that an increase in the polynomial order

Table 3
CIP of a sphere with seven elements

p	CPU time (s)	Dof	Number of GPs	Total number of unknowns
3	2.39	50	112	946
4	3.18	128	175	1528
5	5.37	188	252	2204
6	8.87	262	343	3006
7	14.67	350	448	3934
8	24.13	452	567	4988
9	38.68	568	700	6168
10	59.38	698	847	7474

The order of Gauss–Legendre integration is chosen $p + 1$ in each spatial direction.
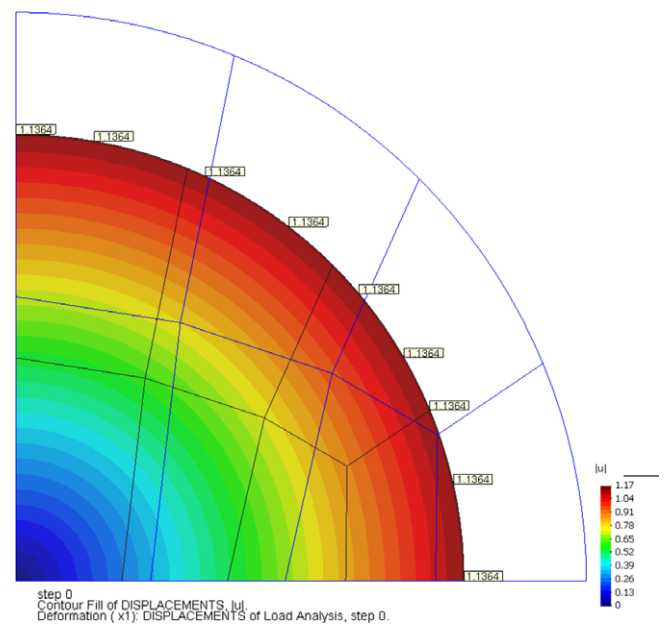
Fig. 11. Cold isostatic pressing of a sphere, here seven elements, $p = 3$. For a pressure of 500 MPa the displacement along the surface is $|\vec{u}| = 1.1671$, the relative density throughout the domain 0.88753. After unloading the remaining displacement is $|\vec{u}| = 1.1364$ and the relative density 0.86631.
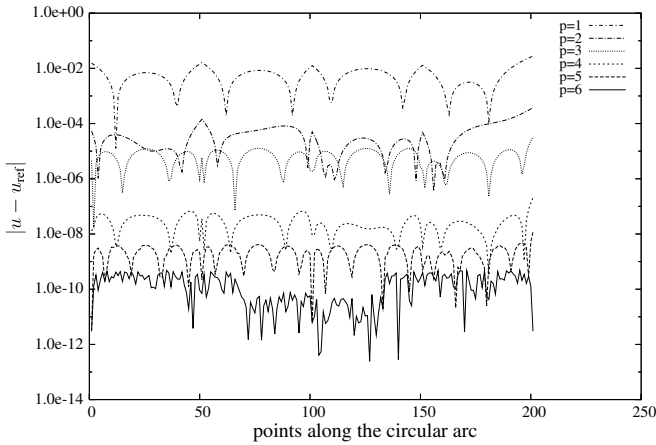
Fig. 12. Influence of the polynomial degree on the deviation $|u - u_{ref}|$ in the displacement along the circular arc after compaction with 500 MPa.

of the shape functions corresponds to an increase in the accuracy of the representation of the circular arc of at least one order.

4.2.2. CIP of a powder cylinder with a rigid spherical inset

This example models a 'complex' experiment where uniaxial die-compaction is followed by cold isostatic pressing (CIP). The experimental setup and simulation with an explicit h-version code is described in detail in [35]. Here the calculations are done applying the p-version. A steel sphere is embedded in a cylinder of copper powder that is compressed. This inset causes an inhomogeneous defor-

mation in the body. The final body is shown in Fig. 13. Fixing the position of the sphere embedded in the powder inside the CIP chamber is very difficult. Therefore as a first step uniaxial pre-compaction of the specimen with the sphere inside is done. This brittle body is carefully transferred to the CIP unit where the isostatic pressure is applied.

4.2.3. Modeling the process

The procedure of the experiment suggests to split the modeling of the process into four stages (Fig. 14).

(1) Die-compaction with displacement control. The experimental data is compiled in [35]. The initial height reported there corresponds to a relative density of 0.376 for the copper domain. As the material parameters for the constitutive model were determined for pre-compacted powder with initial relative density of 0.42, the initial height corresponding to this relative density was calculated by purely geometrical considerations from the powder mass, the known volume of the steel sphere, density of copper and the dimensions of the cylindrical die. For the numerical simulation we use the resulting initial height of 29.55 mm.

After die-compaction the body has an average height of 23.482 mm. A corresponding deformation of 6.068 mm is prescribed to model this stage. The rotational symmetry allows to use axisymmetric elements and as the origin is placed in the center of
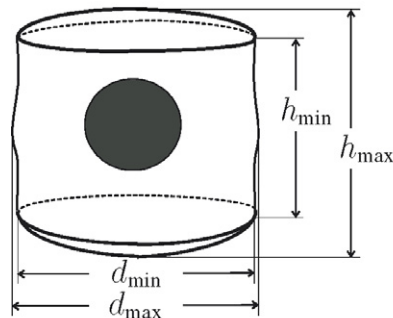
Fig. 13. Cut specimen after the experiment. The minimum and maximum diameter and height are available for comparison with the simulation.
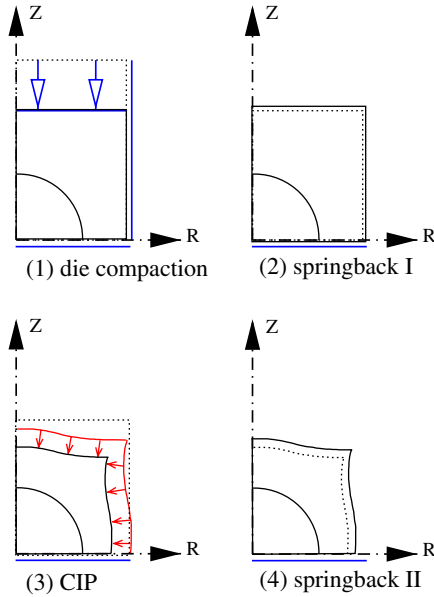
Fig. 14. Schematic representation of the four stages. Displacement perpendicular to the blue lines is clamped or prescribed as in (1). Dotted lines represent the shape at the start of the stage, solid lines at the end: (1) die-compaction; (2) springback I; (3) CIP; (4) springback II. (For interpretation of the references in color in this figure legend, the reader is referred to the web version of this article.)

the sphere only a quarter of the longitudinal plane has to be modeled setting symmetry boundary conditions as shown in Fig. 15. Hence the initial height of the computational domain is 14.775 mm and the radius of the body is 10.015 mm. A deformation $\bar{u}_z = -3.034$ mm is prescribed at the upper edge. The left and right edges are fixed in radial direction ($\bar{u}_r = 0$), while the bottom edge is clamped in axial direction ($\bar{u}_z = 0$). Calculations showed that the rigid

steel sphere is numerically equivalent to a clamped circular arc because it is much stiffer than the copper powder. Consequently, the calculations reported here were carried out with the arc clamped, i.e. along the arc $\bar{u}_r = 0, \bar{u}_z = 0$.

(2) Springback I: The final state of the die-compaction is the starting configuration for the springback stage where only symmetry boundary conditions are set and the reaction forces induced by the prescribed displacements of stage 1 are reduced to zero.

(3) CIP: The body from stage 2 is subjected to isostatic pressure of 300 MPa acting on the current deformed configuration (follower loading) of the outer boundary.

(4) Springback II: Also after CIP there is springback where the load is taken away. What remains is the overall "plastic" (remaining) deformation.

For the simulation a coarse mesh as shown in Fig. 16 is used. Again the curved boundary is described by the blending function method. Counting from the arc in the lower left corner we distinguish three layers of elements where different polynomial degrees may be set as shown in Fig. 16.

The numerical simulation follows the four stages explained above. The state at the end of each run (displacement vectors of all elements, internal variables at all Gauss points) is the starting configuration for the following stage with the new boundary conditions. The rate-independent version of the constitutive model ($\eta = 0$) was used for comparison with the calculations of [35]. Different polynomial degree distributions were investigated. Comparing the numerically obtained dimensions to the experimental values we find that the difference is below 3.5% and the moderate computation time as indicated in Table 4 allows to apply the simulation to gain insight into the process. Tak-

Fig. 15. Cross section of the initial geometry in cylindrical coordinates and the reduced axisymmetric system with symmetry boundary conditions. The geometric dimensions are $a = 10.015$ mm ($2a = 20.03$ mm), $b = 14.775$ mm ($2b = 29.55$ mm) and the steel sphere has a diameter of 11.89 mm (radius $r = 5.945$ mm). The z-axis coincides with the axis of rotation.
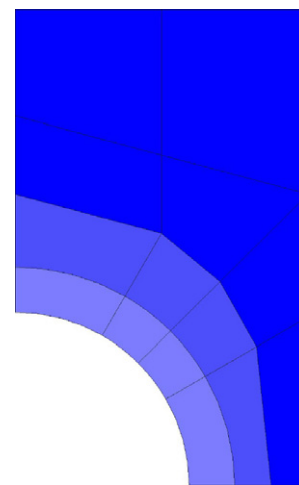
Fig. 16. Coarse p-version mesh. The colors group the three areas where different Ansatz orders may be set. For example $p = 4$-8-10 codes for $p = 4$ in the region adjacent to the arc, $p = 8$ in the next layer and $p = 10$ in the remaining elements.

Table 4
Specimen dimensions (mm) after the entire process

Dimensions after release of pressure				H_{min}	H_{max}	D_{min}	D_{max}
Experiment (mean value)				21.092	21.304	17.348	17.614
Standard deviation				0.062	0.015	0.020	0.024
Numerical results							
Run	Dof	Int. vars.	$\sum$CPU (s)				
$p = 2$	29	882	37.88	20.4437 (3.07%)	20.9088 (1.86%)	17.9495 (3.47%)	18.0834 (2.66%)
$p = 3$	143	1568	78.32	20.4379 (3.10%)	20.8741 (2.02%)	17.9430 (3.43%)	18.0965 (2.74%)
$p = 4$	228	2450	150.15	20.4369 (3.11%)	20.8811 (1.99%)	17.9398 (3.41%)	18.1071 (2.80%)
$p = 5$	341	3528	278.69	20.4386 (3.10%)	20.8852 (1.97%)	17.9375 (3.40%)	18.1132 (2.83%)
$p = 2\text{-}4\text{-}6$	330	3010	295.31	20.4394 (3.09%)	20.8929 (1.93%)	17.9456 (3.44%)	18.0862 (2.68%)
$p = 2\text{-}6\text{-}8$	576	5026	837.61	20.4399 (3.09%)	20.8912 (1.94%)	17.9453 (3.44%)	18.0864 (2.68%)
$p = 3\text{-}6\text{-}8$	584	5222	878.79	20.4426 (3.08%)	20.8876 (1.95%)	17.9418 (3.42%)	18.0968 (2.74%)
$p = 4\text{-}6\text{-}8$	600	5474	944.73	20.4391 (3.10%)	20.8867 (1.96%)	17.9392 (3.41%)	18.1057 (2.79%)
$p = 4\text{-}8\text{-}10$	926	8050	2514.59	20.4398 (3.09%)	20.8877 (1.95%)	17.9388 (3.41%)	18.1054 (2.79%)

Comparison of experiment [35] and FE results. The CPU time includes all four stages of the process. The number in brackets is the relative difference between the experiment and the FE result in %.
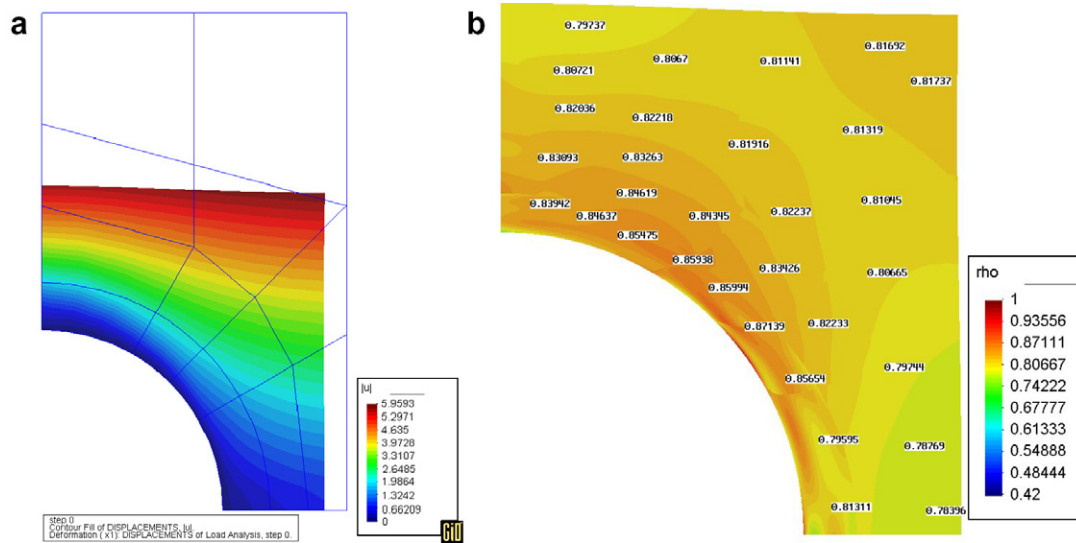
Fig. 17. Displacement and distribution of relative density after the entire process: (a) undeformed mesh and deformation $|u|$; (b) spatial distribution of the relative density in the powder ($p = 5$ in all elements).

ing into account that no friction was modeled this is a very good agreement. It is interesting to note that in [35] the same constitutive model is used within an explicit h-version code. The dimensions after the process match the experimental results very well, however, the calculation times were in the magnitude of days.

In our implicit approach it proved vital to implement an automatic control of the stepsize. Since the load-deflection slope at the beginning of the loading process is very flat, small loading steps have to be used. On the other hand as the material gets denser the stepsize can be increased. The deformed body and the distribution of the relative density at the end of the process is shown in Fig. 17. The relative density along a cutline from the center of the sphere to the top right corner (in reference configuration) in Fig. 18 allows to rate the quality of the approximation. As the relative density depends on the determinant of the deformation gradient, i.e. on derivatives of the displace-
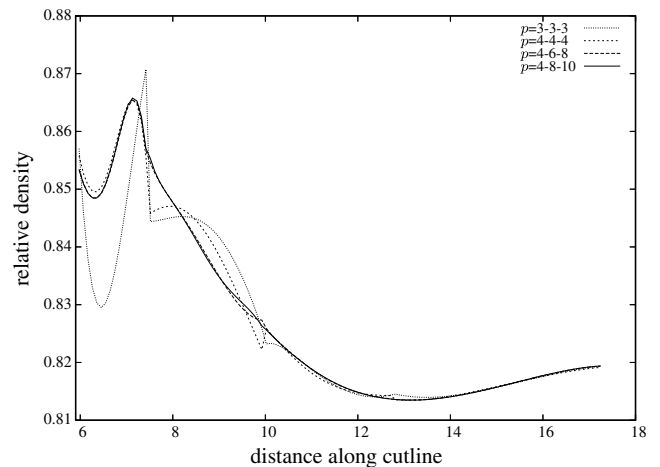
Fig. 18. Convergence of the relative density along a cutline from the center of the arc to the top right corner (in reference configuration) for different polynomial patterns.

ment, there may be discontinuities over element boundaries as the displacement field is only C^0 continuous there. These discontinuities are an indicator for the accuracy – analogous to arguments used in error estimators based on recovery methods, see for example [29]. For the uniform polynomial degree pattern $p = 4\text{-}4\text{-}4$, i.e. $p = 4$ in each of the three layers of elements shown in Fig. 16, a discontinuity is visible that is smoothed if the polynomial degree for the second and third layer of elements is raised using $p = 4\text{-}6\text{-}8$ indicating an improvement. If the polynomial order is raised to $p = 4\text{-}8\text{-}10$ an almost smooth curve is obtained.

5. Conclusion

We demonstrate that simulating powder compaction processes by an implicit high order finite element code is feasible with good accuracy and offers an alternative to the dominating explicit *h*-version approach. In [30] the use of explicit codes for powder compaction is partially attributed to problems caused by element distortion. This is no obstacle for the *p*-version as its robustness regarding element distortion is well known [34]. One further obstacle may be that constitutive models with ordinary differential equations governing the evolution of the yield function can become very difficult to solve numerically. This was investigated in [18] and strategies were proposed to overcome this problem that made the computations reported here possible. For constitutive models with internal variables the additional unknowns at each spatial quadrature point – seven for the applied model – must be taken into account when choosing a discretization strategy as they are associated with a significant share of computation time. The benefit of the *p*-version approach for the investigated geometric and material nonlinear applications is a faster convergence in terms of unknowns compared to low order *h*-refinement. The return of investment for increasing the polynomial order and using more complicated element stiffness matrices and data structures justifies the effort also with respect to computation time.

Acknowledgements

References

[1] A. Abbo, S. Sloan, A smooth hyperbolic approximation to the Mohr–Coulomb yield criterion, Comput. Struct. 54 (1995) 427–441.

[2] F. Armero, A. Perez-Foguet, On the formulation of closest-point projection algorithms in elastoplasticity – Part I: The variational structure, Int. J. Numer. Methods Engrg. 53 (2002) 331–374.

[3] M. Arnold, K. Frischmuth, Solving problems with unilateral constraints by DAE methods, Math. Comput. Simul. 47 (1998) 47–67.

[4] M. Aubertin, L. Li, A porosity-dependent inelastic criterion for engineering materials, Int. J. Plast. 20 (2004) 2179–2208.

[5] U. Banerjee, M. Suri, The effect of numerical quadrature in the *p*-version of the finite element method, Math. Comput. 59 (199) (1992) 1–20.

[6] W. Bier, M. Dariel, N. Frage, S. Hartmann, O. Michailov, Die compaction of copper powder designed for material parameter identification, Int. J. Mech. Sci. 49 (2007) 766–777.

[7] W. Bier, S. Hartmann, A finite strain constitutive model for metal powder compaction using a unique and convex single surface yield function, Eur. J. Mech., Series A/Solids 25 (2006) 1009–1030.

[8] D. Bigoni, A. Piccolroaz, Yield criteria for quasibrittle and frictional materials, Int. J. Solids Struct. 41 (2004) 2855–2878.

[9] T. Davis, I. Duff, Umfpack version 2.2 unsymmetric-pattern multifrontal package, 1997. http://heron.cc.ukans.edu/software/umfpack.

[10] A. Düster, S. Hartmann, E. Rank, *p*-FEM applied to finite isotropic hyperelastic bodies, Comput. Methods Appl. Mech. Engrg. 192 (2003) 5147–5166.

[11] A. Düster, E. Rank, The *p*-version of the finite element method compared to an adaptive *h*-version for the deformation theory of plasticity, Comput. Methods Appl. Mech. Engrg. 190 (2001) 1925–1935.

[12] A. Düster, E. Rank, A *p*-version finite element approach for two- and three-dimensional problems of the J_2 flow theory with non-linear isotropic hardening, Int. J. Numer. Methods Engrg. 53 (2002) 49–63.

[13] W. Ehlers, A single-surface yield function for geomaterials, Arch. Appl. Mech. 65 (1995) 246–259.

[14] P. Ellsiepen, S. Hartmann, Remarks on the interpretation of current non-linear finite-element-analyses as differential-algebraic equations, Int. J. Numer. Methods Engrg. 51 (2001) 679–707.

[15] W. Gordon, C. Hall, Construction of curvilinear co-ordinate systems and applications to mesh generation, Int. J. Numer. Methods Engrg. 7 (1973) 461–477.

[16] S. Hartmann, Finite-Elemente Berechnung inelastischer Kontinua – Interpretation als Algebro-Differentialgleichungssysteme. Postdoctoral Thesis, Institut für Mechanik, Universität Kassel, 2003.

[17] S. Hartmann, A remark on the application of the Newton–Raphson method in non-linear finite element analysis, Comput. Mech. 36 (2) (2005) 100–116.

[18] S. Hartmann, W. Bier, High-order time integration applied to metal powder plasticity, Int. J. Plast., in press, doi:10.1016/j.ijplas.2007.01.014.

[19] P. Haupt, Continuum Mechanics and Theory of Materials, second ed., Springer, Berlin, 2002.

[20] P. Haupt, C. Tsakmakis, On the application of dual variables in continuum mechanics, J. Contin. Mech. Thermodyn. 1 (1989) 165–196.

[21] P. Haupt, C. Tsakmakis, Stress tensors associated with deformation tensors via duality, Arch. Mech. 48 (1996) 347–384.

[22] U. Heißerer, S. Hartmann, A. Düster, Z. Yosibash, On volumetric locking-free behavior of *p*-version finite elements under finite deformations. Commun. Numer. Methods Engrg., in press. doi:10.1002/cnm.1008.

[23] S. Holzer, Z. Yosibash, The *p*-version of the finite element method in incremental elasto-plastic analysis, Int. J. Numer. Methods Engrg. 39 (1996) 1859–1878.

[24] B. Jeremic, C. Xenophontos, Application of the *p*-version of the finite element method to elasto-plasticity with localization of deformation, Commun. Numer. Methods Engrg. 15 (2) (1999) 867–876.

[25] R. Krause, R. Mücke, E. Rank, *hp*-version finite elements for geometrically nonlinear problems, Commun. Numer. Methods Engrg. 11 (1995) 887–897.

[26] G. Kreisselmeier, R. Steinhauser, Systematische Auslegung von Reglern durch Optimierung eines vektoriellen Gütekriteriums, Regelungstechnik 3 (1979) 76–79.

[27] L. Mähler, M. Ekh, K. Runesson, A class of thermo-hyperelastic–viscoplastic models for porous materials: theory and numerics, Int. J. Plast. 17 (7) (2001) 943–969.

[28] A. Perez-Foguet, F. Armero, On the formulation of closest-point projection algorithms in elastoplasticity – Part II: Globally convergent schemes, Int. J. Numer. Methods Engrg. 53 (2002) 331–374.

[29] E. Rank, O. Zienkiewicz, A simple error estimator in the finite element method, Commun. Appl. Numer. Methods 3 (1987) 243–249.

[30] H. Riedel, T. Kraft, Simulation in powder technology, in: D. Raabe, F. Roters, F. Barlat, L.-Q. Chen (Eds.), Continuum Scale Simulation of Engineering Materials: Fundamentals – Microstructures – Process Applications, Wiley-VCH Verlag, 2004, pp. 73–490 (Chapter 26).

[31] J.C. Simo, K.S. Pister, Remarks on rate constitutive equations for finite deformation problems: computational implications, Comput. Methods Appl. Mech. Engrg. 46 (1984) 201–215.

[32] B. Szabó, R. Actis, S. Holzer, Solution of elastic–plastic stress analysis problems by the *p*-version of the finite element method, in: I.

Babuška, J. Flaherty (Eds.), Modeling, Mesh Generation, and Adaptive Numerical Methods for Partial Differential Equations, IMA Volumes in Mathematics and its Applications, vol. 75, Springer, New York, 1995, pp. 395–416.

[33] B. Szabó, I. Babuška, Finite Element Analysis, John Wiley & Sons, 1991.

[34] B. Szabó, A. Düster, E. Rank, The *p*-version of the finite element method, in: E. Stein, R. de Borst, T. Hughes (Eds.), Encyclopedia of Computational Mechanics, John Wiley & Sons, 2003.

[35] M. Szanto, W. Bier, N. Frage, S. Hartmann, Z. Yosibash, Experimental based finite element simulation of cold isostatic pressing of metal powders. Int. J. Mech. Sci., submitted for publication.

[36] Z. Yosibash, S. Hartmann, U. Heisserer, A. Düster, E. Rank, M. Szanto, Axisymmetric pressure boundary loading for finite deformation analysis using *p*-FEM, Comput. Methods Appl. Mech. Engrg. 196 (2007) 1261–1277.